Chemical Science

ROYAL SOCIETY OF CHEMISTRY

EDGE ARTICLE

View Article Online
View Journal | View Issue

Cite this: *Chem. Sci.*, 2024, **15**, 10969

All publication charges for this article have been paid for by the Royal Society of Chemistry

Received 22nd March 2024
Accepted 7th June 2024

DOI: 10.1039/d4sc01916d

rsc.li/chemical-science

Dual-modal imaging-guided agent based on NIR-II aggregation-induced emission luminogens with balanced phototheranostic performance†

Chengjun Dong, ‡[a] Ziwen Zhang,‡[b] Hongyu Wu,[b] Xinting Liang,[a] Shihao Pang,[a] Kehuan Wu,[b] Jie Sun,[a] Xuemei Dong,[a] Lixin Sun,[a] Xianfeng Gu *[b] and Chunchang Zhao *[a]

Phototherapy has garnered considerable interest for its potential to revolutionize conventional cancer treatment. Organic materials with near-infrared II (NIR-II, 1000–1700 nm) fluorescence and photothermal effects are key for precise tumor diagnosis and treatment, yet optimizing their output for higher resolution and reduced photodamage remains a challenge. Herein, a multifunctional NIR-II photosensitizer (**LSC**) has been developed using the aggregation-induced emission (AIE) technology. The utilization of thieno[3,2-*b*]thiophene as an electron-rich and bulky donor/acceptor bridge has allowed for the elongation of conjugation length and distortion of the AIE main chain. This strategic modification effectively enhances the electron push–pull effect, endowing the **LSC** with a Stokes shift of over 400 nm and AIE characteristics. We have successfully built-up stable nanoparticles called **FA-LSC NPs** using a nano-precipitation method. These nanoparticles exhibit high NIR-II fluorescent brightness ($\varepsilon \times QY = 1064\ M^{-1}\ cm^{-1}$) and photothermal conversion efficiency (41%). Furthermore, the biocompatible **FA-LSC NPs** demonstrate effective tumor accumulation and exceptional photothermal therapeutic efficacy both *in vitro* and *in vivo*. These nanoparticles were applied to fluorescence-photothermal dual-mode imaging-guided photothermal ablation in a HeLa tumor xenograft mouse model, resulting in favorable photothermal clearance outcomes.

Introduction

Cancer poses a significant risk to human health due to its propensity for metastasis, rapid dissemination, and high fatality rates. Although conventional clinical interventions like surgery and chemotherapy have made notable progress, the intricate structures and complex mechanisms of tumors contribute to substantial adverse effects associated with these treatment modalities.[1–3] Phototheranostics represents a cutting-edge, non-invasive diagnostic and therapeutic strategy that facilitates real-time diagnosis and concurrent *in situ* treatment triggered by light activation. This technique offers several advantages, including high spatiotemporal selectivity, low toxicity, minimal invasiveness, high efficacy, and robust controllability, thereby paving the way for innovative cancer research.[4–10] In contrast, a single organic molecule-based multimodal phototheranostic system offers a compelling alternative to conventional multimodal systems, owing to its simplicity, ease of synthesis, well-defined structure, excellent biocompatibility, and high reproducibility.[11–14] To address the challenge of effectively treating hypoxic tumors, photothermal therapy (PTT) can eliminate cancer cells in both normoxic and hypoxic environments, irrespective of the oxygen concentration.[15–19] Consequently, the development of photothermal therapy within the NIR-II window becomes imperative as it enables deeper tissue penetration due to reduced absorption and scattering, thereby offering a promising avenue for effectively treating deeply-seated hypoxic tumors.[20–23]

At present, the emission spectra of most organic fluorophores are predominantly situated within the visible light range or the first near-infrared window (NIR-I, 650–900 nm), in which imaging is significantly hampered by pronounced photon scattering and intrinsic autofluorescence in biological tissues.[24–28] Recent research has highlighted the advantages of fluorescence imaging in the second near-infrared window (NIR-II, 1000–1700 nm), including deeper tissue penetration, improved resolution, and reduced background interference. Organic small molecule probes are attractive owing to their

[a]*Key Laboratory for Advanced Materials and Feringa Nobel Prize Scientist Joint Research Center, Institute of Fine Chemicals, School of Chemistry and Molecular Engineering, East China University of Science and Technology, Shanghai, 200237, P. R. China. E-mail: zhaocchang@ecust.edu.cn*

[b]*Department of Medicinal Chemistry, School of Pharmacy, Fudan University, Shanghai, 201203, P. R. China*

† Electronic supplementary information (ESI) available: Procedures for synthesis, characterization data, and supplementary figures. See DOI: https://doi.org/10.1039/d4sc01916d

‡ These authors contributed equally.

straightforward synthesis and ease of metabolization. Nonetheless, conventional probes with rigid planar aromatic structures unavoidably facilitate π–π stacking and intrinsic fluorescence quenching *via* the aggregation-caused quenching (ACQ) effect. Due to their suboptimal fluorescence brightness, practical applications have been hindered. The primary factors influencing the fluorescence brightness of fluorescent dyes are the molar extinction coefficient (MEC) and quantum yield (QY). In response to the prevalent ACQ effect, considerable effort has been devoted to incorporating aggregation-induced emission (AIE) functionalities.[29–34] However, the limited availability of high quantum yield NIR-II fluorescent groups currently impedes the full exploitation of imaging penetration depth in this spectral range,[35–43] Therefore, this has driven us to develop a singular AIE NPs that possesses both effective NIR-II window imaging and PTT capabilities.

Herein, we report a strategy that integrates high NIR-II fluorescence brightness ($\varepsilon \times QY > 1000\ M^{-1}\ cm^{-1}$) and photothermal performance into a single AIEgen (Scheme 1). In this design, we have opted for the *N*,*N*-diaryl dihydrophenazine (DPZ) fragment due to its dual function as a strong electron donor and a molecular rotor. Moreover, the twisted conformation of the DPZ fragment prolongs the intermolecular distance, leading to relatively loose molecular stacking even in its aggregated state. This assists in maintaining partial intramolecular rotation, thereby facilitating heat generation within the NPs. We first fabricate a benz[*cd*]indol-2(1*h*)-one-based derivative DC. Due to strong electronic push–pull effect, it exhibited intense NIR-I absorption and NIR-II emission with a Stokes shift of 347 nm. It showed pronounced AIE characteristics in a DMSO/toluene system but contributed minimally in photothermal effects. Subsequently, we introduced a thiophene segment as a π-bridge between DPZ and indolium salt derivatives. The incorporation of the thiophene ring was also aimed at expanding the molecular distance between the DPZ unit and the large-volume electron acceptor, further facilitating intramolecular rotation and the efficiency of photothermal conversion in the aggregated state.[44–49] The intramolecular charge transfer (ICT) effect was significantly enhanced due to the extension of the donor and an increase in the degree of donor–acceptor (D–A) conformational distortion, with the Stokes shifts of **SC** and **LSC** expanded to 444 nm and 465 nm,

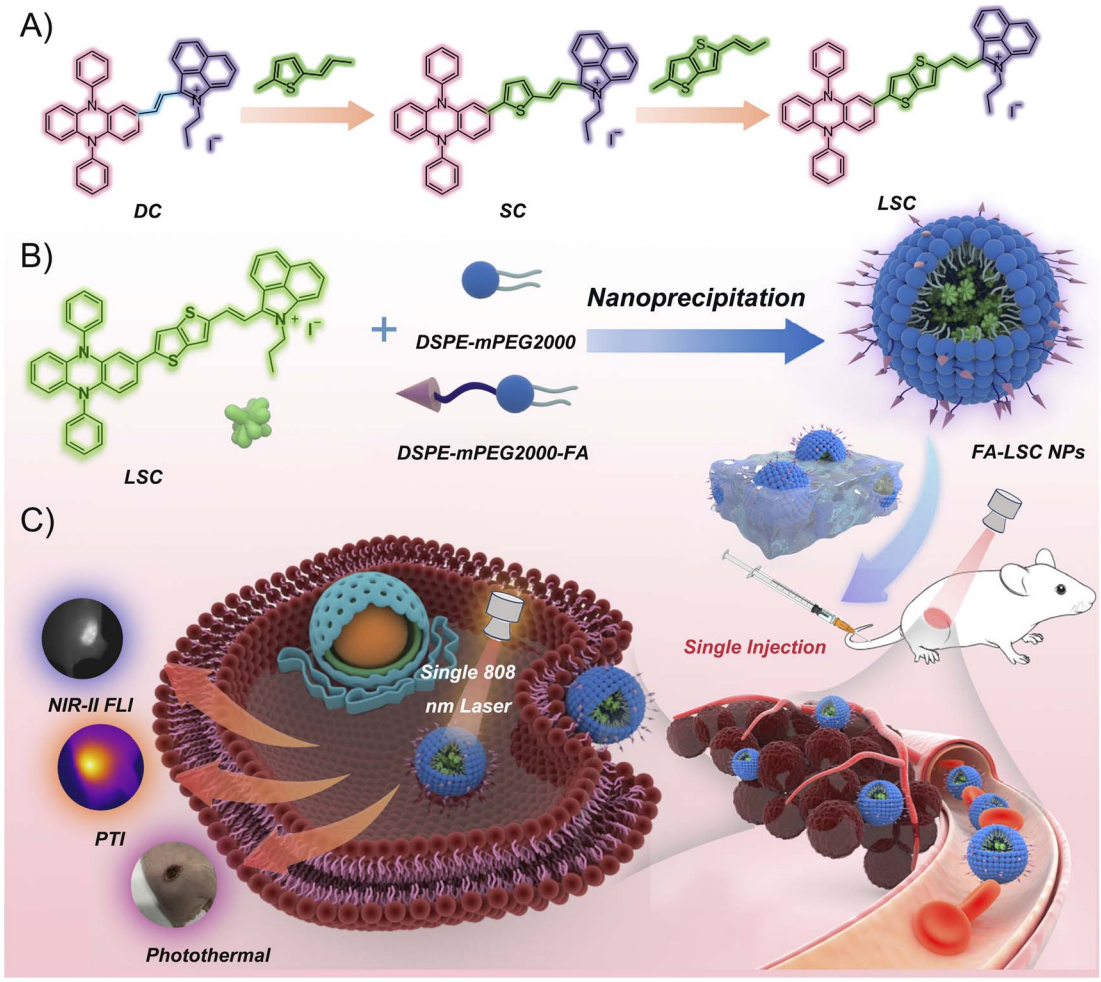

Scheme 1 The molecular structures, nanofabrication and versatile phototheranostic application. (A) Molecular structures of designed compounds including **DC**, **SC** and **LSC**. (B) Preparation of **FA-LSC NPs** by a nanoprecipitation method. (C) Illustration of the reconciled photophysical processes and application of **FA-LSC NPs** on NIR-II FLI- PTI imaging-guided PTT synergistic cancer therapy.

respectively. Additionally, the introduction of the thiophene ring is expected to increase the molecular distance between the DPZ unit and the bulky electron acceptor, further promoting intramolecular rotation and enhancing the photothermal conversion efficiency in the aggregated state. In addition, the prepared **FA-LSC NPs** exhibit ideal blood circulation, demonstrating excellent stability, photothermal conversion ability, and acceptable fluorescence quantum yield. It is reasonable to believe that **LSC** compounds with high D–π–A strength and intramolecular motion are the most promising photothermal molecules. Both *in vitro* and *in vivo* studies have confirmed the tumor eradication of HeLa tumor-bearing mice through fluorescence imaging-guided PTT using **FA-LSC NPs**. In summary, this study provides a novel D–π–A configuration molecular design by regulating compound torsional structures to reduce intermolecular π–π stacking, offering insights into the design of anti-quenching fluorescent groups.

Results and discussion

Molecular design, synthesis, and theoretical calculation

The designed compounds can be obtained through simple synthetic steps, and the synthetic routes for these compounds are provided in ESI (ESI).† In brief, the reduction of phenazine with sodium thiosulfate gave the structure of dihydrophenazine. Subsequently, treatment of dihydrophenazine with brominated aromatics, palladium acetate, tributyl phosphine, and sodium *n*-butoxide in toluene under reflux conditions led to the production of *N*,*N*-diaryl dihydrophenazine (DPZ). Then, the Suzuki coupling reactions using **4** and pre-synthesized thiophene intermediates **1** and **5** (SBr and LSBr) are performed to extend the π-conjugation of the donor DPZ, resulting in high-yielding (up to 85%) bridge donors **6** and **7**. Finally, aldehyde intermediates **6** and **7** are individually reacted with benzoindole salt derivative **3** in ethanol solution *via* a simple Knoevenagel condensation reaction to obtain the corresponding **SC** and **LSC** with yields ranging from 75% to 85%. The structures of the products are satisfactorily characterized (Fig. S1–24†).

Density functional theory (DFT) and time-dependent DFT (TD-DFT) simulations on **DC**, **SC** and **LSC** molecules are first performed to understand their photophysical properties (Fig. 1B and S28†). The calculated highest occupied molecular orbitals (HOMOs), lowest unoccupied molecular orbitals (LUMOs), and the geometry after optimization are depicted as shown in the Fig. 1. For three D–π–A structured molecules, the electron density at the LUMO energy level is predominantly localized on the electron-deficient benzo[*c*,*d*]indolium ring and the bridging π-bonds, whereas the electron density at the HOMO level is primarily concentrated around the electron-rich DPZ framework (Fig. 1C). In addition, **LSC** achieves an ICT efficiency of 95.4%, which is higher than **DC** (70.4%) and **SC** (82.3%). Therefore, the Stokes shift of **LSC** (465 nm) in DMSO is much larger than that of **DC** (347 nm) and **SC** (444 nm). The geometric relaxation of the molecule provides a pathway for generating heat upon excitation, which is advantageous for photothermal therapy.

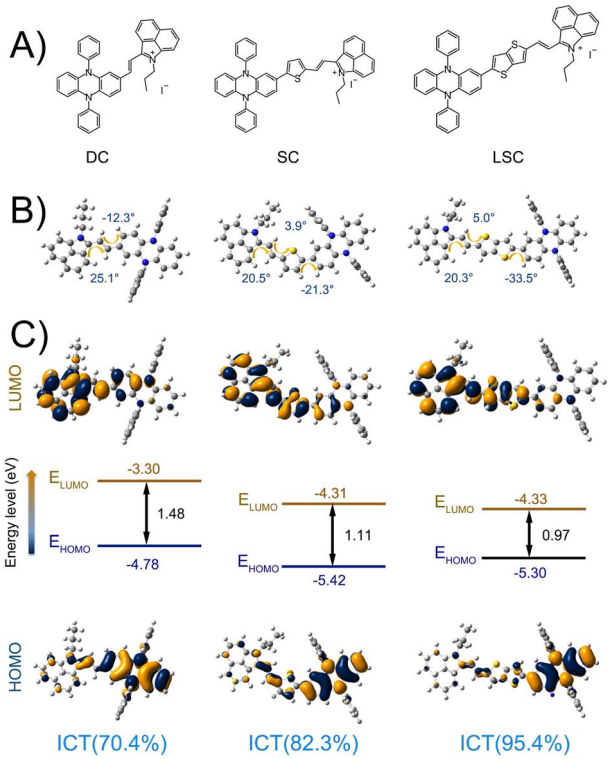

Fig. 1 Structure details of **DC**, **SC** and **LSC**. (A) Chemical structures. (B) Optimized S_0 geometries. (C) Illustration of the frontier molecular orbitals (LUMOs and HOMOs) of singlet-state (S_1) geometries determined at the B3LPY/6-31G (d, p) TD level of theory.

Photophysical properties

The optical properties of **DC**, **SC** and **LSC** were studied using UV-vis-NIR and photoluminescence spectroscopy systems. Their maximum absorption peaks in dimethyl sulfoxide (DMSO) were observed at 918 nm, 871 nm, and 821 nm, respectively. Notably, three molecules exhibited remarkably broad absorption ranges from 650 nm to 1250 nm, with high absorption rates even at the long-wavelength region of 808 nm. As shown in Fig. 2A, the **LSC** molecules show a shorter-wavelength absorption than the **DC** molecules while their emissions lie in the same region beyond 1000 nm, demonstrating a large Stokes shift of 465 nm for **LSC** molecules (Fig. S26 and S27†). The maximum emission peaks of **DC**, **SC** and **LSC** in toluene were located at 1148 nm, 1238 nm, and 1275 nm, respectively, which is in complete agreement with the bandgap calculated based on optimized singlet state geometries. Due to the predominant emission in the NIR-II region, **DC**, **SC** and **LSC** hold great potential for NIR-II fluorescence-guided phototherapy using near-infrared laser excitation.

Hydrophobic molecules are often assembled into water-dispersible NPs to enhance colloidal stability and *in vivo* circulation time. The alteration in exciton dynamics following nano coalescence can lead to a change in the inherent properties of the monomers. Therefore, a clear understanding of the aggregated state properties is essential for further biological applications. To further investigate the optical properties, we

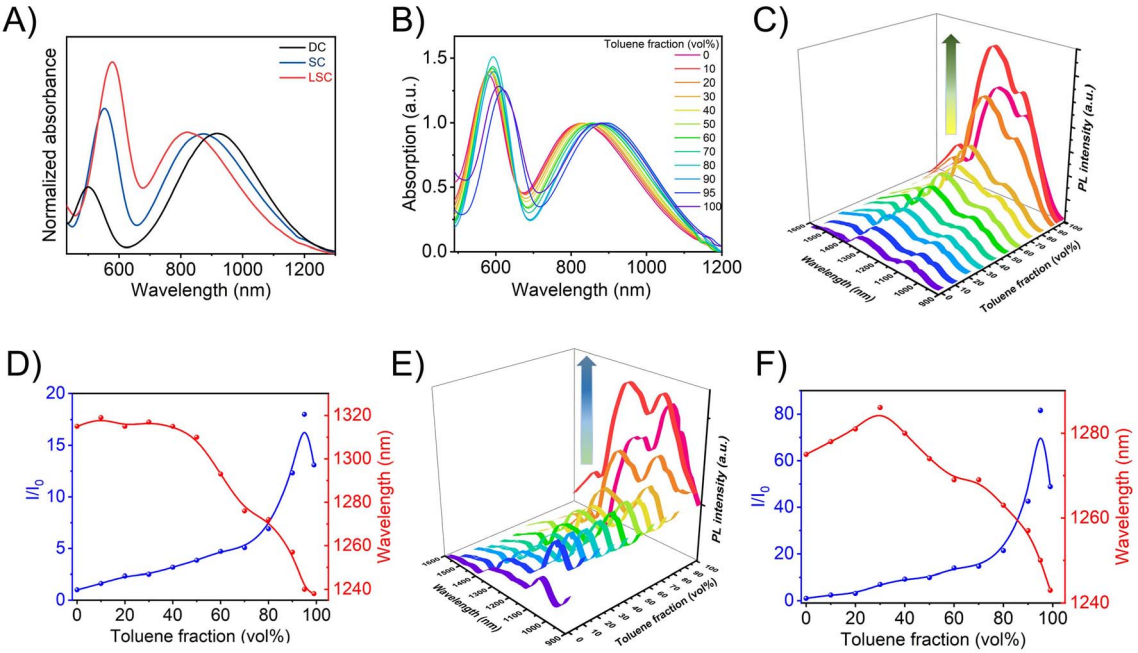

Fig. 2 Characterization and properties of the obtained compounds. (A) Normalized absorption spectra of compounds in DMSO solution (10×10^{-6} M). (B) Absorption spectra **LSC** (10×10^{-6} M) in the mixture of toluene/DMSO with different fractions of toluene (f_T). Photoluminescence (PL) spectra of 10×10^{-6} M (C) **SC** and (E) **LSC** in the mixture of DMSO/toluene with different fractions of toluene (f_T). (λ_{ex}: 808 nm). Plot of the relative emission intensity (I/I_0) of (D) **SC** and (F) **LSC** with toluene fraction. I_0 and I are the peak values of PL intensities of AIEgens (10×10^{-6} M) in DMSO and DMSO/toluene mixtures, respectively.

measured the spectral characteristics of three compounds in DMSO/toluene mixtures with varying toluene fractions (f_T). As shown in Fig. 2B, the absorption peak of **LSC** red shifts from 819 to 891 nm when the f_T increases from 0 to 95%. The results imply that **LSC** form aggregates which is featured with red-shifted absorption in the aggregated state. The three compounds exhibit markedly weak emission in DMSO/toluene mixtures ranging from 0–60% (Fig. 2B–F and S32†). As the toluene fraction increases, the fluorescence intensity of **DC**, **SC**, and **LSC** significantly enhances due to the restriction of rotor rotation, indicating their AIE properties (Fig. S31†). Taking **LSC** for example, with the increase in toluene fraction (from 0 to 95%), the emission intensity of **LSC** at 1286 nm initially decreased slightly, then the spectra showed a hypsochromic shift from 1286 to 1243 nm, followed by a dramatic increase in fluorescence intensity. At a toluene content of 95%, the fluorescence intensity reached its maximum, and at 99% toluene content, the intensity slightly decreased. However, the fluorescence intensity was still 48 times higher than that in solution, demonstrating typical AIE characteristics.

Characterization and properties of NPs

To fabricate AIE NPs with excellent biocompatibility, targeted functionality, and good dispersibility, a nano-precipitation method was employed to directly encapsulate **DC**, **SC** and **LSC** within the amphiphilic copolymer DSPE-mPEG2000-FA. The UV-vis-NIR absorption and fluorescence spectra of the as prepared NPs located at 852, 859, and 825 nm, respectively (Fig. 3B and S33†). The average sizes of the resulting **FA-DC**, **FA-SC** and **FA-LSC NPs** were determined to be approximately 21, 27 and 30 nm, respectively, through dynamic light scattering (DLS) measurements (Fig. 3A). Moreover, transmission electron microscopy (TEM) images demonstrated uniform morphologies of these NPs, with diameters around 25 nm (Fig. S40†). Interestingly, the TEM measurements suggested a slightly smaller size compared to the hydrodynamic diameter values obtained from DLS, which could be attributed to the absence of a hydration layer on the NPs surface. Additionally, the zeta potentials of **FA-DC NPs**, **FA-SC NPs** and **FA-LSC NPs** were determined to be −17 mV, −15 mV and −30 mV, respectively (Fig. S39†). It is worth noting that after one week of storage under ambient conditions, there were no significant changes in the particle size and absorbance of the AIE NPs in PBS, indicating their excellent colloidal stability (Fig. S38 and 39†). The emission peak of **FA-LSC NPs** extends beyond 1200 nm (Fig. 3C), which is advantageous for *in vivo* bioimaging. Emission intensities of **FA-LSC NPs** dispersion with different concentrations are further measured under 808 nm laser excitation (Fig. S29†). The results indicate that the NIR-II fluorescence signal of **FA-LSC NPs** increases linearly with concentration, demonstrating their capability for quantitative imaging.

To evaluate the NIR-II emission capability of the NPs, the relative QYs in the NIR-II region in aqueous solution were determined using IR-26 (QY = 0.5%) as a reference (Fig. 3E and S41†). The fluorescence quantum yield of **LSC** in water dropped rapidly to 0.008%, whereas the quantum yield of **FA-LSC NPs** in water increased by nearly 160 times. The NIR-II fluorescence brightness, the main criterion for imaging performance

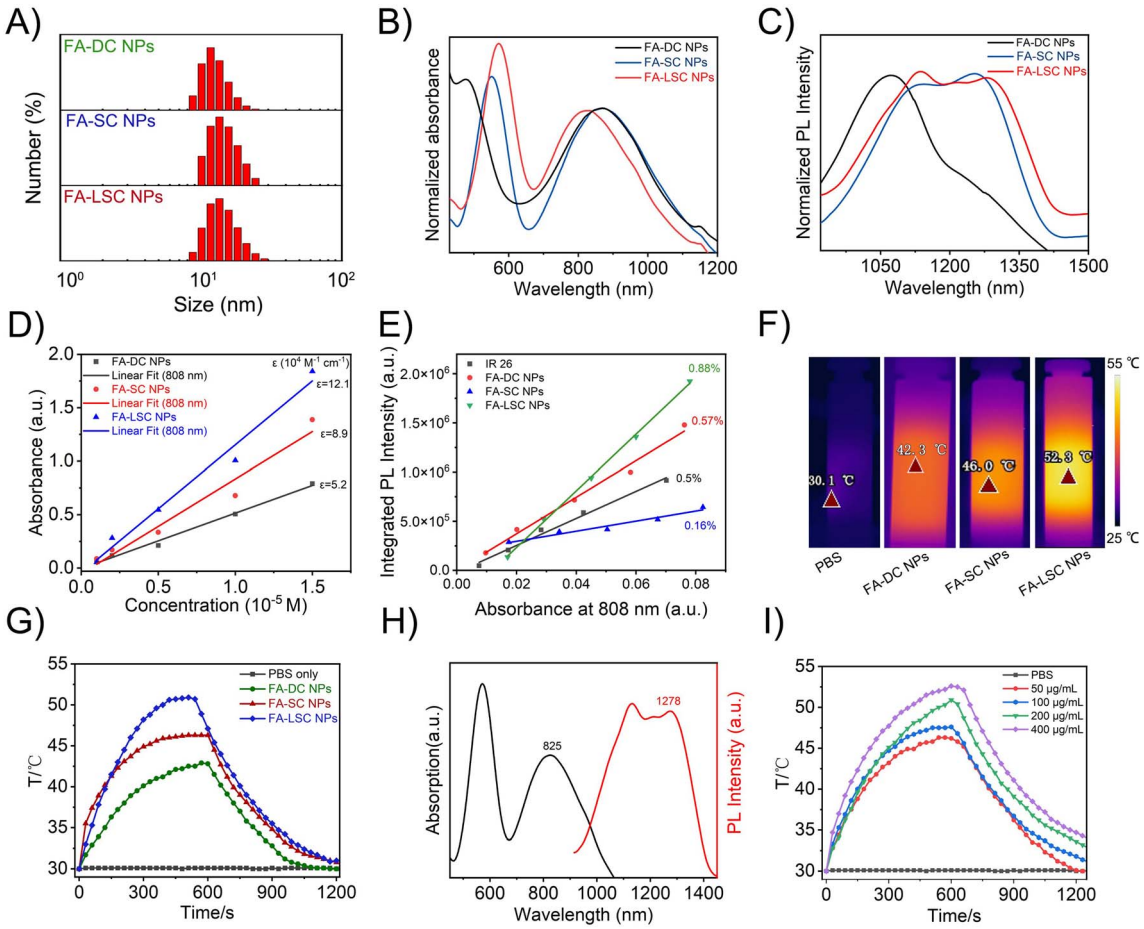

Fig. 3 (A) Size distributions of corresponding NPs. (B) Normalized absorption and (C) normalized emission spectra of these NPs in aqueous solution. (D) The values of ε at their major absorption peaks. (E) The integrated fluorescence spectra (1000–1500 nm) of different samples *versus* different absorbance at 808 nm (IR-26, QY = 0.5% in dichloroethane). (F) The corresponding IR thermal images under different conditions at 10 min post-irradiation. (G) Comparison of the photothermal conversion behavior of the compounds in aqueous solution (200 μg mL^{-1}) under 808 nm laser irradiation. (H) The absorption (blank line) and emission (red line) spectra of **FA-LSC NPs** in aqueous solution. (I) Concentration-dependent temperature change of **FA-LSC NPs** in aqueous solution.

evaluation in fluorescent molecules, was assessed based on $\varepsilon \times$ QY values. The values of ε at 808 nm absorption peaks were determined to be 1.21×10^5 M^{-1} cm^{-1} for **FA-LSC NPs**, 0.89×10^5 M^{-1} cm^{-1} for **FA-SC NPs** and 0.52×10^5 M^{-1} cm^{-1} for **FA-DC NPs** (Fig. 3D). Under excitation with an 808 nm laser in the aqueous solution, the emission peaks of **FA-DC NPs**, **FA-SC NPs**, and **FA-LSC NPs** are located at approximately 1074 nm, 1257 nm, and 1278 nm, respectively. Accordingly, the $\varepsilon \times$ QY values of **FA-DC NPs**, **FA-SC NPs** and **FA-LSC NPs** at 808 nm absorption peak wavelengths were calculated to be 296.4, 142.4 and 1064.8, respectively (Table S1†). The calculated result for **FA-LSC NPs** is significantly higher than most previously reported NIR-II fluorophores.[50–53]

The photothermal effect of the NPs was subsequently evaluated. Next, photothermal conversion behaviors of the three NPs in PBS solution were recorded by the temperature change over the irradiation time. As illustrated in Fig. 3F and G, the temperatures of the molecules rapidly increased and reached their plateaus after 600 s of the proper laser irradiation, with the heat generation efficiency in the order of **FA-LSC NPs** > **FA-SC NPs** > **FA-DC NPs**. To be specific, the temperature of **FA-LSC NPs** (200 μg mL^{-1}) solution reached a maximum at 52.3 °C with a 22.3 °C temperature increase (ΔT) when irradiated using the 808 nm laser, which is much higher than that of **FA-DC NPs** ($\Delta T \approx 12$ °C) and **FA-SC NPs** ($\Delta T \approx 16$ °C) under 808 nm laser illumination (Fig. S37†). The photothermal conversion efficiency of **FA-LSC NPs** was found to be as high as 41%. This indicates that the molecules within the NPs are highly active and in an aggregated state. Furthermore, the impact of laser power density was also estimated. There is a positive correlation between the photothermal effect of **FA-DC NPs**, **FA-SC NPs** and **FA-LSC NPs** and the laser power density (Fig. S34–36†). This correlation suggests that the generation of heat can be effectively regulated and controlled (Fig. 3I). The results demonstrate that **FA-LSC NPs** exhibit notable photothermal stability, as they maintain their excellent performance even after undergoing consecutive heating and cooling cycles for four times. In contrast, the clinically utilized indocyanine green displays significant photothermal instability (Fig. S36†).

In vitro tumoricidal studies

Thereupon, we investigated the NIR-II laser-induced tumoricidal effects of **FA-LSC NPs** toward HeLa tumor cells by CCK-8 assay (Fig. 5A and B). First, **FA-LSC NPs** were found no obvious toxicity to HeLa tumor cells as well as normal cells (RAW264.7) even at a high concentration under dark, indicating the extraordinary biocompatibility. Subsequently, the active targeting capability of FA-ICG NPs was evaluated using fluorescence imaging in HeLa cells, which are known to highly express folate receptors. As commercial fluorescence confocal microscopy and flow cytometry lack detection channels for **FA-LSC NPs**, indocyanine green (ICG) was used as a substitute for **LSC** in this experiment to validate the *in vitro* targeting ability of **FA-LSC NPs**. As depicted in Fig. 4, the fluorescence intensity in the FA-ICG NPs treatment group was higher compared to the other two groups (PEG-ICG NPs treatment group and FA + FA-ICG NPs treatment group). Conversely, there was a noticeable difference in cellular uptake of FA-ICG NPs in MCF-7 cells, which lack the FA receptor (Fig. S42 and 43†). These findings indicate that **FA-LSC NPs** can actively target cells expressing the FA receptor through endocytosis.

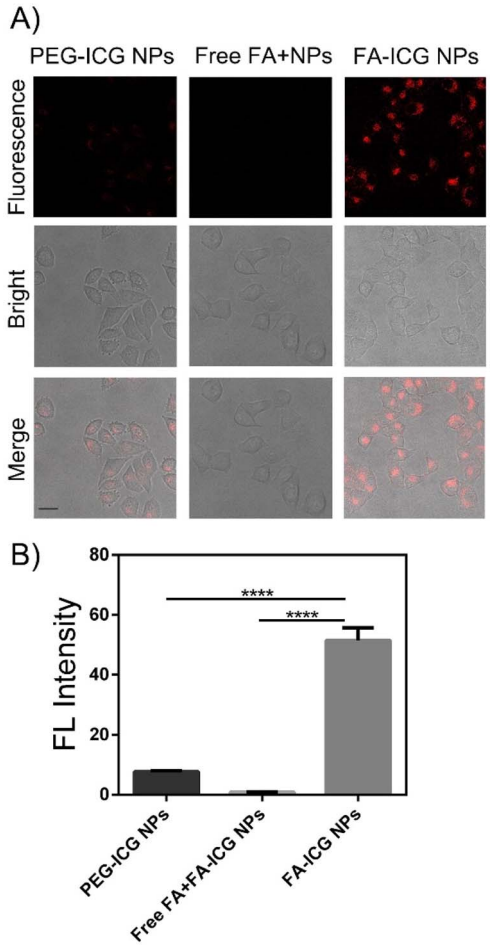

Fig. 4 (A) Confocal fluorescence imaging of HeLa cells uptake of PEG-ICG NPs, free FA + FA-ICG NPs and FA-ICG NPs (order from left to right). $C_{ICG} = 200\ \mu g\ mL^{-1}$ (in DMEM), Scale bar: 20 μm. (B) Relative fluorescence intensities quantified from images in (A). ****$p < 0.0001$.

Considering the favorable photothermal performance of **FA-LSC NPs**, we further quantitatively assessed their cytotoxicity against HeLa cells. As shown in the Fig. 5C, even in the presence of 400 μg mL^{-1} **FA-LSC NPs**, the impact on cell viability remained minimal, with a cell survival rate of 98% in the dark. These results highlight the excellent biocompatibility and low cytotoxicity of **FA-LSC NPs**. After irradiation with 808 nm laser (2 W cm^{-2}) for 8 min, HeLa cells treated with **FA-LSC NPs** exhibited dose-dependent apoptosis. With increasing irradiation time, the cell viability assay gradually revealed cytotoxicity. In contrast, neither the laser irradiation alone group nor the **FA-LSC NPs** alone group was able to eliminate cancer cells. These results demonstrate that the combination of **FA-LSC NPs** and laser irradiation effectively induces apoptosis in HeLa cells, highlighting the synergistic therapeutic effect of photothermal therapy. To investigate the changes in the NIR-I fluorescence of the probe under different treatment conditions, confocal microscopy and flow cytometry were employed. A staining experiment using calcein-AM (green fluorescence for live cells) and PI (red fluorescence for dead cells) was conducted to evaluate the efficacy of the photothermal therapy in killing tumor cells. This allowed us to assess the effectiveness of the nanomaterials in inducing cell death. In the Fig. 5E and S44,† cells treated with laser irradiation alone or **FA-LSC NPs** alone did not show significant cell death. However, when incubated with **FA-LSC NPs** and subsequently exposed to long-term 808 nm laser irradiation (8 min), the cell images displayed intense red fluorescence and negligible green fluorescence. This indicates that the cells treated with **FA-LSC NPs** exhibited strong tumor-killing effects under the conditions of laser irradiation. These results further support the potent therapeutic efficacy of **FA-LSC NPs** in combination with laser treatment. Furthermore, flow cytometry experiments revealed that cells co-treated with nanoparticles and laser exhibited early apoptosis within a short period of time. This cytotoxic effect was mainly attributed to cell apoptosis, as evidenced by the results shown in Fig. 5D and F. In conclusion, these findings provide compelling evidence that **FA-LSC NPs** can effectively target HeLa cells through active internalization and induce cancer cell death through localized hyperthermia, thus offering a promising approach for targeted therapy. *In vivo* evaluation of photothermal treatment.

The goal of our research is to develop integrated diagnostic and therapeutic probes for accurate tumor diagnosis and *in vivo* tumor eradication. In this study, we evaluated the effectiveness of **FA-LSC NPs**-mediated *in vivo* dual-mode imaging-guided therapy. The experimental procedure involved implanting tumors in nude mice (Fig. 6A), allowing them to grow for 8 days before treatment. After a treatment period of 14 days, the mice were euthanized for analysis. We first administered **FA-LSC NPs** to HeLa tumor-bearing nude mice *via* tail vein injection, followed by successfully capturing NIR-II fluorescence imaging signals after 6 hours post-injection. Initially, under the illumination of a 1100 nm long-pass filter, the mice exhibited minimal spontaneous fluorescence, indicating a negligible level of background interference. Subsequently, upon intravenous injection of **FA-LSC NPs**, a gradual and significant enhancement in the NIR-II fluorescence signal intensity was observed at the

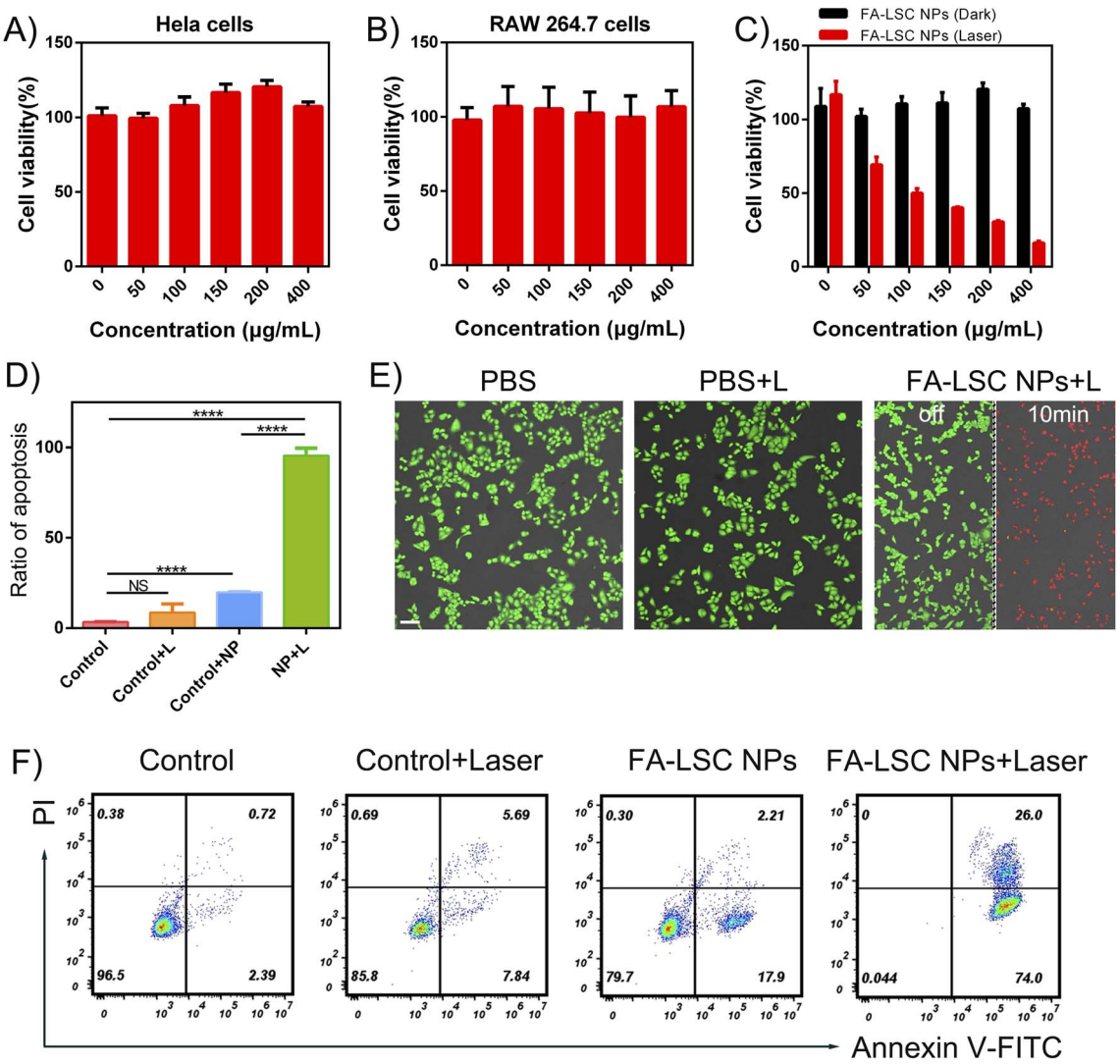

Fig. 5 Cell viability of (A) HeLa cells and (B) RAW 264.7 cells after incubation with **FA-LSC NPs** of different concentrations without 808 nm laser irradiation. *In vitro* PTT cellular tumoricidal performance. Cell viability of (C) HeLa cells after incubation with **FA-LSC NPs** of different concentrations with (red column) or without (dark column) 808 nm laser irradiation (2 W cm^{-2} for 8 min, $n = 5$). (D) Relative fluorescence intensities quantified from images in (F). (E) Live/dead images of HeLa cells after various treatments. The green fluorescence from calcein-AM and red fluorescence from PI represent live cell and dead cells, respectively. Scale bars: 50 μm. (F) Flow cytometry quantification of annexin V-FITC and PI-labeled HeLa cells treated with PBS, **FA-LSC NPs**, without irradiation; PBS + L and **FA-LSC NPs** + L under 808 nm irradiation respectively (200 μg mL^{-1}, 808 nm, 2 W cm^{-2}, 8 min). ****$p < 0.0001$.

tumor site. This fluorescence signal became detectable after 6 hours and reached its peak at 12 hours, suggesting a robust accumulation of **FA-LSC NPs** in the tumor. However, a gradual decline in the fluorescence signal was observed after 24 hours, likely attributed to metabolic processes (Fig. 6B). These findings provide compelling evidence for the potent tumor-targeting ability of **FA-LSC NPs** *in vivo*. To further investigate the *in vivo* distribution of **FA-LSC NPs**, the mice were euthanized 12 hours post-injection, and NIR-II fluorescence images of various organs and tumor tissues were acquired, accompanied by quantitative analysis. Notably, a distinct fluorescence signal was observed specifically in the tumor region (Fig. S47†). To verify the PTT potential of **FA-LSC NPs**, *in vivo* photothermal assessments were then carried out on the subcutaneous Hela-bearing mice under 808 nm laser (2 W cm^{-2}) irradiation. After a single intravenous injection of **FA-LSC NPs** for 12 h, infrared thermography clearly depicted a rapid increase in the tumor site temperature from 34.0 °C to 49.8 °C within 3 min of laserirradiation (Fig. 6C). Subsequently, the temperature climbed to a plateau at approximately 59.9 °C after 10 min period of 808 nm laser exposure (Fig. S45†). In contrast, only a slight elevation ($\Delta T = 2.7$ °C) was observed in the PBS-injected mice, indicating the negligible influence on temperature rise by the laser only.

In vivo PTT was conducted after 12 hours tail vein injection of **FA-LSC NPs** by using 808 nm laser illumination (2 W cm^{-2}) for 10 min. During the period of 14 days treatments, tumor volumes and body weight of all groups were measured every 2 days. As displayed in Fig. 6D, the PBS, PBS + L, and AIE NPs

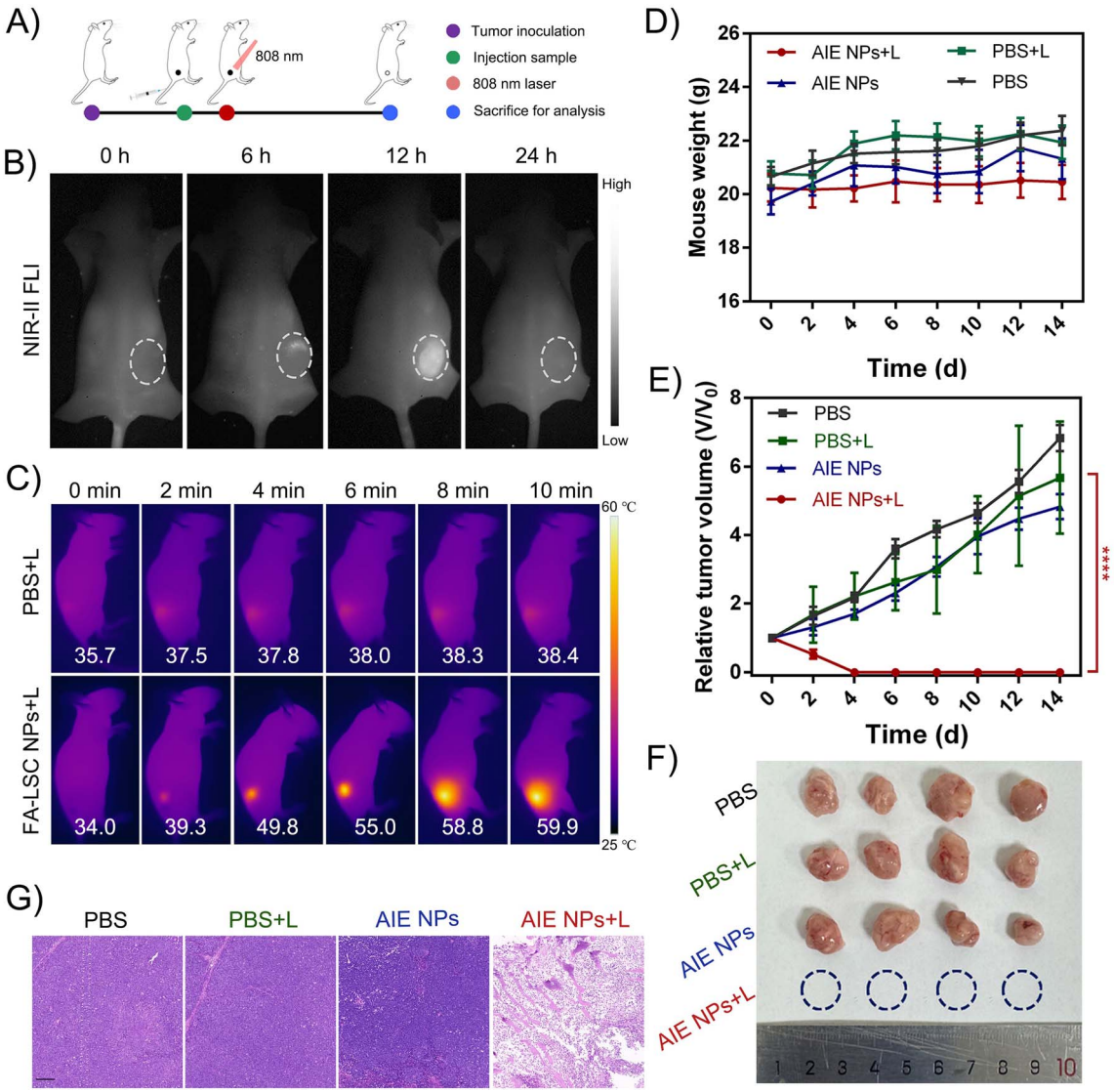

Fig. 6 *In vivo* multimodal imaging-guided photothermal therapeutic efficiency of **FA-LSC NPs** in HeLa tumor-bearing mice. (A) Schematic illustration of the tumor treatment. (B) NIR-II FLI and (C) PTI of HeLa tumor-bearing mice after intravenous injection of **FA-LSC NPs** at different monitoring times. (D) Body weight curves and (E) tumor growth of HeLa tumor-bearing mice during the treatment process. (F) Photos of the tumors harvested at day 14 after different treatments. (G) Histological H&E staining analysis of HeLa tumor-bearing mice under different treatment processes $n = 5$. Scale bar: 100 μm. AIE NPs on behalf of **FA-LSC NPs**. ****$p < 0.0001$.

groups exhibited a rapid increase in tumor volume throughout the study period. As a sharp contrast, for the AIE NPs + L group, significant tumor growth inhibition was observed in the following 14 days post-treatment. These findings indicate that neither laser irradiation alone nor administration of **FA-LSC NPs** alone exerted any inhibitory effect on tumor growth. Excitingly, treatment with **FA-LSC NPs** photothermal therapy led to complete eradication of solid tumors in mice. Remarkably, by the third day post-treatment, virtually no visible tumors were observed. After a 14 days treatment period, the tumors were eliminated without any signs of recurrence, leaving behind only scar tissue (Fig. S46†). Neither treatment-induced substantial alterations in body weight nor mouse death was observed over the course of 14 days treatments (Fig. 6E), demonstrating the good biocompatibility of **FA-LSC NPs** preliminarily. These compelling findings underscore the remarkable therapeutic efficacy of **FA-LSC NPs**. Consequently, the tumor-selective delivery of **FA-LSC NPs** and their site-specific photothermal effect hold tremendous promise for NIR-II/PTI-based tumor diagnosis and treatment, while minimizing the risk of thermal damage to healthy organs and cells.

At the end of the 14 days treatment period, mice from all experimental groups were dissected for histopathological analysis. Tumor tissues and major organs (heart, liver, spleen, lung, and kidney) were collected and subjected to staining with hematoxylin and eosin to evaluate the potential pathological damage induced by **FA-LSC NPs**. Comparison between mice treated with **FA-LSC NPs** in combination with laser irradiation and the control groups revealed a complete absence of tumor tissue samples in the **FA-LSC NPs** + laser treatment group

(Fig. 6F). Furthermore, mice treated with only laser irradiation and **FA-LSC NPs** displayed no significant histopathological damage at the tumor site (Fig. 6G). Additionally, H&E images of the major organs in the treatment group exhibited minimal tissue pathology (Fig. S48†). These findings collectively indicate the excellent biocompatibility and *in vivo* safety of **FA-LSC NPs**. Furthermore, tumor slices from different groups were subjected to tunel staining, which revealed that **FA-LSC NPs** phototherapy successfully induced apoptosis in the tumor site (Fig. S49†). Finally, negligible changes in body weight were observed in all mice during the treatment period, underscoring the high efficacy and minimal side effects of **FA-LSC NPs** for image-guided photothermal therapy.

Conclusions

In summary, we have developed a series of novel single AIE fluorophores as phototherapeutic agents based on a *N*,*N*-diaryl dihydrophenazine moiety with anti-quenching properties for highly efficient *in vivo* bioimaging and cancer phototheranostics. Utilizing intramolecular rotation, twisted conformation, and high D–π–A intensity, the AIE molecule-based agents cleverly achieve a balance between radiative and non-radiative energy dissipation. The molecular design strategy could simultaneously achieve a large Stokes shift and AIE effect. These two features efficiently resolve the quenching issues of previously reported NIR-II J-aggregates and provide bright emission beyond 1200 nm and a large Stokes shift of 465 nm in **FA-LSC NPs**. Moreover, **FA-LSC NPs** can also generate heat under 808 nm laser irradiation for cancer phototherapy (41%). *In vivo* evaluations clearly indicate that **FA-LSC NPs** can synergistically enable NIR-II fluorescence imaging and photothermal imaging for precise tracking of cervical cancer tumors in mice. Single 808 nm laser irradiation in both *in vivo* and *in vitro* experiments strongly demonstrate the high therapeutic efficacy of **FA-LSC NPs** in NIR-II fluorescence imaging-guided photothermal therapy. Thus, this study exemplifies a new approach to designing J-aggregate NIR-II emitters with precisely controlled photophysical properties. The results of this study provide a new case for the design of a multifunctional platform for cancer phototherapy and offer new strategies for highly efficient cancer photothermal immunotherapy.

Data availability

All relevant data is presented in the paper and ESI.†

Author contributions

C. Dong and Z. Zhang carried out synthesis, characterizations and data collection. H. Wu, X. Liang and K. Wu carried out data curation. S. Pang performed computational simulations and the corresponding description in the manuscript. J. Sun, X. Dong and L. Sun carried out validation. All the authors discussed the results and commented on the manuscript and have given approval to the final version.

Conflicts of interest

There are no conflicts to declare.

Acknowledgements

We gratefully acknowledge financial support by the National Natural Science Foundation of China (22077030, 22271092, 82173657), the Shanghai Municipal Science and Technology Major Project (Grant 2018SHZDZX03) We thank the Research Center of Analysis and Test of East China University of Science and Technology for the help on the characterization.

Notes and references

1 Y. Wang, S. Xu, L. Shi, C. Teh, G. Qi and B. Liu, Cancer-Cell-Activated in situ Synthesis of Mitochondria-Targeting AIE Photosensitizer for Precise Photodynamic Therapy, *Angew. Chem., Int. Ed.*, 2021, **60**, 14945–14953.
2 P. Pei, T. Liu, W. Shen, Z. Liu and K. Yang, Biomaterial-mediated internal radioisotope therapy, *Mater. Horiz.*, 2021, **8**, 1348–1366.
3 R. Wang, K. Yin, M. Ma, T. Zhu, J. Gao, J. Sun, X. Dong, C. Dong, X. Gu, H. Tian and C. Zhao, Alkaline Phosphatase-Initiated Sensitive Responsiveness of Activatable Probes to Hydrogen Sulfide for Accurate Cancer Imaging and Differentiation, *CCS Chem.*, 2022, **4**, 3715–3723.
4 S. Goel, D. Ni and W. Cai, Harnessing the Power of Nanotechnology for Enhanced Radiation Therapy, *ACS Nano*, 2017, **11**, 5233–5237.
5 P. Zhu, Y. Chen and J. Shi, Nanoenzyme-Augmented Cancer Sonodynamic Therapy by Catalytic Tumor Oxygenation, *ACS Nano*, 2018, **12**, 3780–3795.
6 S. Son, J. Kim, J. Kim, B. Kim, J. Lee, Y. Kim, M. Li, H. Kang and J. S. Kim, Cancer therapeutics based on diverse energy sources, *Chem. Soc. Rev.*, 2022, **51**, 8201–8215.
7 Q. Yu, X. Li, J. Wang, L. Guo, L. Huang and W. Gao, Recent Advances in Reprogramming Strategy of Tumor Microenvironment for Rejuvenating Photosensitizers-Mediated Photodynamic Therapy, *Small*, 2023, e2305708, DOI: 10.1002/smll.202305708.
8 V. N. Nguyen, Z. Zhao, B. Z. Tang and J. Yoon, Organic photosensitizers for antimicrobial phototherapy, *Chem. Soc. Rev.*, 2022, **51**, 3324–3340.
9 T. I. Valerio, C. L. Furrer, N. Sadeghipour, S.-J. X. Patrock, S. A. Tillery, A. R. Hoover, K. Liu and W. R. Chen, Immune modulations of the tumor microenvironment in response to phototherapy, *J. Innovative Opt. Health Sci.*, 2023, **16**, 2330007.
10 D. An, J. Fu, B. Zhang, N. Xie, G. Nie, H. Ågren, M. Qiu and H. Zhang, NIR-II Responsive Inorganic 2D Nanomaterials for Cancer Photothermal Therapy: Recent Advances and Future Challenges, *Adv. Funct. Mater.*, 2021, **31**, 2101625.
11 H. Dai, Q. Shen, J. Shao, W. Wang, F. Gao and X. Dong, Small Molecular NIR-II Fluorophores for Cancer Phototheranostics, *Innovation*, 2021, **2**, 100082.

12 H. Lou, A. Ji, C. Qu, H. Liu, L. Jiang, H. Chen and Z. Cheng, A Small-Molecule Based Organic Nanoparticle for Photothermal Therapy and Near-Infrared-IIb Imaging, *ACS Appl. Mater. Interfaces*, 2022, **14**, 35454–35465.

13 L. Li, Y. Liu, T. Sun, T. Zhou, Y. Bai, X. Liu, S. Zhang, T. Jia, X. Zhao and Y. Wang, An "all-in-one" strategy based on the organic molecule DCN-4CQA for effective NIR-fluorescence-imaging-guided dual phototherapy, *J. Mater. Chem. B*, 2021, **9**, 5785–5793.

14 H. Li, Q. Li, Y. Gu, M. Wang, P. Tan, H. Wang, L. Han, Y. Zhu, F. He and L. Tian, Dimerization extends π-conjugation of electron donor-acceptor structures leading to phototheranostic properties beyond the sum of two monomers, *Aggregate*, 2024, **28**, e528.

15 H. Wang, K. F. Xue, Y. Yang, H. Hu, J. F. Xu and X. Zhang, In Situ Hypoxia-Induced Supramolecular Perylene Diimide Radical Anions in Tumors for Photothermal Therapy with Improved Specificity, *J. Am. Chem. Soc.*, 2022, **144**, 2360–2367.

16 H. Sun, Q. Zhang, J. Li, S. Peng, X. Wang and R. Cai, Near-infrared photoactivated nanomedicines for photothermal synergistic cancer therapy, *Nano Today*, 2021, **37**, 101073.

17 Y. Zou, W. Liu, W. Sun, J. Du, J. Fan and X. Peng, Highly Inoxidizable Heptamethine Cyanine–Glucose Oxidase Conjugate Nanoagent for Combination of Enhanced Photothermal Therapy and Tumor Starvation, *Adv. Funct. Mater.*, 2022, **32**, 2111853.

18 W. Wang, Y. Gao, W. Xu, Y. Xu, N. Zhou, Y. Li, M. Zhang and B. Z. Tang, The One-Stop Integrated Nanoagent Based on Photothermal Therapy for Deep Infection Healing and Inflammation Inhibition, *Adv. Mater.*, 2024, **36**, e2307785.

19 P. Sun, F. Qu, C. Zhang, P. Cheng, X. Li, Q. Shen, D. Li and Q. Fan, NIR-II Excitation Phototheranostic Platform for Synergistic Photothermal Therapy/Chemotherapy/Chemodynamic Therapy of Breast Cancer Bone Metastases, *Adv. Sci.*, 2022, **9**, e2204718.

20 Y. Gao, Y. Li, Z. Xu, S. Yu, J. Liu and H. Sun, Multiporphyrinic architectures: Advances in structural design for photodynamic therapy, *Aggregate*, 2023, **5**, e420.

21 Z. H. Wu, M. Peng, C. Ji, P. Kardasis, I. Tzourtzouklis, M. Baumgarten, H. Wu, T. Basche, G. Floudas, M. Yin and K. Mullen, A Terrylene-Anthraquinone Dyad as a Chromophore for Photothermal Therapy in the NIR-II Window, *J. Am. Chem. Soc.*, 2023, **145**, 26487–26493.

22 S. Tian, H. Bai, S. Li, Y. Xiao, X. Cui, X. Li, J. Tan, Z. Huang, D. Shen, W. Liu, P. Wang, B. Z. Tang and C. S. Lee, Water-Soluble Organic Nanoparticles with Programable Intermolecular Charge Transfer for NIR-II Photothermal Anti-Bacterial Therapy, *Angew. Chem., Int. Ed.*, 2021, **60**, 11758–11762.

23 P. Wang, J. Li, M. Wei, R. Yang, K. Lou, Y. Dang, W. Sun, F. Xue and X. Liu, Tumor-microenvironment triggered signal-to-noise boosting nanoprobes for NIR-IIb fluorescence imaging guided tumor surgery and NIR-II photothermal therapy, *Biomaterials*, 2022, **287**, 121636.

24 S. Zhu, R. Tian, A. L. Antaris, X. Chen and H. Dai, Near-Infrared-II Molecular Dyes for Cancer Imaging and Surgery, *Adv. Mater.*, 2019, **31**, e1900321.

25 C. Li, G. Chen, Y. Zhang, F. Wu and Q. Wang, Advanced Fluorescence Imaging Technology in the Near-Infrared-II Window for Biomedical Applications, *J. Am. Chem. Soc.*, 2020, **142**, 14789–14804.

26 C. Yin, X. Lu, Q. Fan and W. Huang, Organic semiconducting nanomaterials-assisted phototheranostics in near-infrared-II biological window, *Nanomaterials*, 2020, **2**, 20200070.

27 G. Korotcenkov, Electrospun Metal Oxide Nanofibers and Their Conductometric Gas Sensor Application. Part 2: Gas Sensors and Their Advantages and Limitations, *Nanomaterials*, 2021, **11**, 1555.

28 G. Hong, Y. Zou, A. L. Antaris, S. Diao, D. Wu, K. Cheng, X. Zhang, C. Chen, B. Liu, Y. He, J. Z. Wu, J. Yuan, B. Zhang, Z. Tao, C. Fukunaga and H. Dai, Ultrafast fluorescence imaging in vivo with conjugated polymer fluorophores in the second near-infrared window, *Nat. Commun.*, 2014, **5**, 4206.

29 J. Mei, Y. Hong, J. W. Lam, A. Qin, Y. Tang and B. Z. Tang, Aggregation-induced emission: the whole is more brilliant than the parts, *Adv. Mater.*, 2014, **26**, 5429–5479.

30 Z. Zhao, H. Zhang, J. W. Y. Lam and B. Z. Tang, Aggregation-Induced Emission: New Vistas at the Aggregate Level, *Angew. Chem., Int. Ed.*, 2020, **59**, 9888–9907.

31 D. Yan, Q. Wu, D. Wang and B. Z. Tang, Innovative Synthetic Procedures for Luminogens Showing Aggregation-Induced Emission, *Angew. Chem., Int. Ed.*, 2021, **60**, 15724–15742.

32 D. Yan, Y. Huang, J. Zhang, Q. Wu, G. Song, J. Ji, Q. Jin, D. Wang and B. Z. Tang, Adding Flying Wings: Butterfly-Shaped NIR-II AIEgens with Multiple Molecular Rotors for Photothermal Combating of Bacterial Biofilms, *J. Am. Chem. Soc.*, 2023, **145**, 25705–25715.

33 J. B. Xiong, H. T. Feng, J. P. Sun, W. Z. Xie, D. Yang, M. Liu and Y. S. Zheng, The Fixed Propeller-Like Conformation of Tetraphenylethylene that Reveals Aggregation-Induced Emission Effect, Chiral Recognition, and Enhanced Chiroptical Property, *J. Am. Chem. Soc.*, 2016, **138**, 11469–11472.

34 T. Guo, Y. Lin, D. Pan, X. Zhang, W. Zhu, X. M. Cai, G. Huang, H. Wang, D. Xu, F. E. Kuhn, B. Zhang and T. Zhang, Towards bioresource-based aggregation-induced emission luminogens from lignin beta-O-4 motifs as renewable resources, *Nat. Commun.*, 2023, **14**, 6076.

35 Q. Zhang, P. Yu, Y. Fan, C. Sun, H. He, X. Liu, L. Lu, M. Zhao, H. Zhang and F. Zhang, Bright and Stable NIR-II J-Aggregated AIE Dibodipy-Based Fluorescent Probe for Dynamic In Vivo Bioimaging, *Angew. Chem.*, 2021, **60**, 3967–3973.

36 K. Wei, Y. Wu, X. Zheng, L. Ouyang, G. Ma, C. Ji and M. Yin, A Light-Triggered J-Aggregation-Regulated Therapy Conversion: from Photodynamic/Photothermal Therapy to Long-Lasting Chemodynamic Therapy for Effective Tumor Ablation, *Angew. Chem.*, 2024, e202404395, DOI: **10.1002/anie.202404395**.

37 K. W. Lee, Y. Gao, W. C. Wei, J. H. Tan, Y. Wan, Z. Feng, Y. Zhang, Y. Liu, X. Zheng, C. Cao, H. Chen, P. Wang, S. Li, K. T. Wong and C. S. Lee, Anti-Quenching NIR-II J-

Aggregates of Benzo[c]thiophene Fluorophore for Highly Efficient Bioimaging and Phototheranostics, *Adv. Mater.*, 2023, **35**, e2211632.

38 F. Wurthner, T. E. Kaiser and C. R. Saha-Moller, J-aggregates: from serendipitous discovery to supramolecular engineering of functional dye materials, *Angew. Chem.*, 2011, **50**, 3376–3410.

39 Y. Li, T. Ma, H. Jiang, W. Li, D. Tian, J. Zhu and Z. Li, Anionic Cyanine J-Type Aggregate Nanoparticles with Enhanced Photosensitization for Mitochondria-Targeting Tumor Phototherapy, *Angew. Chem.*, 2022, **61**, e202203093.

40 C. A. Shen, M. Stolte, J. H. Kim, A. Rausch and F. Wurthner, Double J-Coupling Strategy for Near Infrared Emitters, *J. Am. Chem. Soc.*, 2021, **143**, 11946–11950.

41 C. Sun, B. Li, M. Zhao, S. Wang, Z. Lei, L. Lu, H. Zhang, L. Feng, C. Dou, D. Yin, H. Xu, Y. Cheng and F. Zhang, J-Aggregates of Cyanine Dye for NIR-II in Vivo Dynamic Vascular Imaging beyond 1500 nm, *J. Am. Chem. Soc.*, 2019, **141**, 19221–19225.

42 W. Chen, C. A. Cheng, E. D. Cosco, S. Ramakrishnan, J. G. P. Lingg, O. T. Bruns, J. I. Zink and E. M. Sletten, Shortwave Infrared Imaging with J-Aggregates Stabilized in Hollow Mesoporous Silica Nanoparticles, *J. Am. Chem. Soc.*, 2019, **141**, 12475–12480.

43 S. Xu, H.-W. Liu, S.-Y. Huan, L. Yuan and X.-B. Zhang, Recent progress in utilizing near-infrared J-aggregates for imaging and cancer therapy, *Mater. Chem. Front.*, 2021, **5**, 1076–1089.

44 D. Yan, W. Xie, J. Zhang, L. Wang, D. Wang and B. Z. Tang, Donor/pi-Bridge Manipulation for Constructing a Stable NIR-II Aggregation-Induced Emission Luminogen with Balanced Phototheranostic Performance, *Angew. Chem., Int. Ed.*, 2021, **60**, 26769–26776.

45 R. Lan, J. Lv, D. Gao, D. Hu, C. Liu, J. Jia, H. Zheng, C. Liu, P. Zhao and Z. Sheng, Folate Receptor-Targeted NIR-II Dual-Model Nanoprobes for Multiscale Visualization of Macrophages in Rheumatoid Arthritis, *Adv. Funct. Mater.*, 2023, **33**, 2300342.

46 Z. Zhang, W. Xu, M. Kang, H. Wen, H. Guo, P. Zhang, L. Xi, K. Li, L. Wang, D. Wang and B. Z. Tang, An All-Round Athlete on the Track of Phototheranostics: Subtly Regulating the Balance between Radiative and Nonradiative Decays for Multimodal Imaging-Guided Synergistic Therapy, *Adv. Mater.*, 2020, **32**, e2003210.

47 D. Yan, M. Wang, Q. Wu, N. Niu, M. Li, R. Song, J. Rao, M. Kang, Z. Zhang, F. Zhou, D. Wang and B. Z. Tang, Multimodal Imaging-Guided Photothermal Immunotherapy Based on a Versatile NIR-II Aggregation-Induced Emission Luminogen, *Angew. Chem., Int. Ed.*, 2022, **61**, e202202614.

48 J. Li, J. Wang, J. Zhang, T. Han, X. Hu, M. M. S. Lee, D. Wang and B. Z. Tang, A Facile Strategy of Boosting Photothermal Conversion Efficiency through State Transformation for Cancer Therapy, *Adv. Mater.*, 2021, **33**, e2105999.

49 H. Shen, B. Wu, Q. Zhang, J. Ni, M. Liang, Y. Liu, X.-F. Zang, S. Wang, Y.-Y. Quan, X. Ye and Z.-S. Huang, Acceptor/π-bridge planarization and donor rotation manipulation for designing an NIR-II AIEgen with high photothermal conversion efficiency to enhance cancer phototherapy, *Chem. Eng. J.*, 2023, **468**, 143726.

50 A. L. Antaris, H. Chen, S. Diao, Z. Ma, Z. Zhang, S. Zhu, J. Wang, A. X. Lozano, Q. Fan, L. Chew, M. Zhu, K. Cheng, X. Hong, H. Dai and Z. Cheng, A high quantum yield molecule-protein complex fluorophore for near-infrared II imaging, *Nat. Commun.*, 2017, **8**, 15269.

51 H. Shen, F. Sun, X. Zhu, J. Zhang, X. Ou, J. Zhang, C. Xu, H. H. Y. Sung, I. D. Williams, S. Chen, R. T. K. Kwok, J. W. Y. Lam, J. Sun, F. Zhang and B. Z. Tang, Rational Design of NIR-II AIEgens with Ultrahigh Quantum Yields for Photo- and Chemiluminescence Imaging, *J. Am. Chem. Soc.*, 2022, **144**, 15391–15402.

52 Q. Wan, Y. Li, K. Ding, Y. Xie, J. Fan, J. Tong, Z. Zeng, Y. Li, C. Zhao, Z. Wang and B. Z. Tang, Aggregation Effect on Multiperformance Improvement in Aryl-Armed Phenazine-Based Emitters, *J. Am. Chem. Soc.*, 2023, **145**, 1607–1616.

53 Y. Li, Y. Tang, W. Hu, Z. Wang, X. Li, X. Lu, S. Chen, W. Huang and Q. Fan, Incorporation of Robust NIR-II Fluorescence Brightness and Photothermal Performance in a Single Large π-Conjugated Molecule for Phototheranostics, *Adv. Sci.*, 2022, **10**, 2204695.